

Discrepancy between integral and local composition in off-stoichiometric $\text{Cu}_2\text{ZnSnSe}_4$ kesterites: A pitfall for classification

Philipp Schöppe, Galina Gurieva, Sergio Giraldo, Gema Martínez-Criado, Carsten Ronning, Edgardo Saucedo, Susan Schorr, and Claudia S. Schnorr

Citation: *Appl. Phys. Lett.* **110**, 043901 (2017); doi: 10.1063/1.4974819

View online: <http://dx.doi.org/10.1063/1.4974819>

View Table of Contents: <http://aip.scitation.org/toc/apl/110/4>

Published by the [American Institute of Physics](#)


Articles you may be interested in

[Structural transitions of ordered kesterite-type \$\text{Cu}_2\text{ZnSnS}_4\$ under pressure](#)
Appl. Phys. Lett. **110**, 041905041905 (2017); 10.1063/1.4974941

[Modification of defects and potential fluctuations in slow-cooled and quenched \$\text{Cu}_2\text{ZnSnSe}_4\$ single crystals](#)
Appl. Phys. Lett. **121**, 065704065704 (2017); 10.1063/1.4975483

[Controlling metastable native point-defect populations in \$\text{Cu}\(\text{In,Ga}\)\text{Se}_2\$ and \$\text{Cu}_2\text{ZnSnSe}_4\$ materials and solar cells through voltage-bias annealing](#)
Appl. Phys. Lett. **121**, 043102043102 (2017); 10.1063/1.4973959

[Temperature dependent transient surface photovoltage spectroscopy of a \$\text{Cu}_{1.95}\text{Zn}_{1.1}\text{Sn}_{0.96}\text{Se}_4\$ kesterite single phase powder](#)
Appl. Phys. Lett. **110**, 023901023901 (2017); 10.1063/1.4973539



Small Conferences. BIG Ideas.

Applied Physics
Reviews

SAVE THE DATE!
3D Bioprinting: Physical and Chemical Processes
May 2–3, 2017 • Winston Salem, NC, USA

Discrepancy between integral and local composition in off-stoichiometric $\text{Cu}_2\text{ZnSnSe}_4$ kesterites: A pitfall for classification

Philipp Schöppe,¹ Galina Gurieva,² Sergio Giraldo,³ Gema Martínez-Criado,^{4,5} Carsten Ronning,¹ Edgardo Saucedo,³ Susan Schorr,^{2,6} and Claudia S. Schnorr¹

¹*Institut für Festkörperphysik, Friedrich-Schiller-Universität Jena, Max-Wien-Platz 1, 07743 Jena, Germany*

²*Helmholtz-Zentrum Berlin für Materialien und Energie, Hahn-Meitner-Platz 1, 14109 Berlin, Germany*

³*Catalonia Institute for Energy Research (IREC), Jardins de les Dones de Negre 1, 08930 Sant Adrià de Besòs, Barcelona, Spain*

⁴*ESRF—The European Synchrotron, 71 Avenue des Martyrs, 38000 Grenoble, France*

⁵*Instituto de Ciencia de Materiales de Madrid (CSIC), 28049-Cantoblanco, Madrid, Spain*

⁶*Institut für Geologische Wissenschaften, Freie Universität Berlin, Malteserstr. 74–100, 12249 Berlin, Germany*

(Received 21 October 2016; accepted 11 January 2017; published online 23 January 2017)

High-efficiency kesterite-based thin film solar cells typically feature Cu-poor, Zn-rich absorbers although secondary phases occur easily in non-stoichiometric $\text{Cu}_2\text{ZnSnSe}_4$. We therefore applied high-resolution X-ray fluorescence analysis using a synchrotron nanobeam to study the local composition of a CZTSe cross section lamella cut from a sample with an integral composition of $\text{Zn}/\text{Sn} = 1.37$ and $\text{Cu}/(\text{Zn}+\text{Sn}) = 0.55$. We find submicrometer-sized ZnSe-, SnSe/SnSe₂-, and even CuSe/Cu₂Se-like secondary phases, while the local compositions of the kesterite are highly Zn-rich yet barely Cu-poor with $1.5 \leq \text{Zn}/\text{Sn} \leq 2.2$ and $\text{Cu}/(\text{Zn}+\text{Sn}) \sim 1.0$. Consequently, great care must be taken when relating the integral composition to other material properties including the device performance. *Published by AIP Publishing.* [<http://dx.doi.org/10.1063/1.4974819>]

Thin film solar cells based on $\text{Cu}(\text{In,Ga})(\text{Se,S})_2$ absorbers with the chalcopyrite type crystal structure have reached a record efficiency of 22.6%, thus closing the gap to silicon-based technology.¹ However, their large-scale implementation may be hindered by the availability of the rare element In. The so-called kesterite materials, such as $\text{Cu}_2\text{ZnSn}(\text{Se,S})_4$, present an attractive and promising alternative since all elements are non-toxic, low-cost, and earth-abundant, and record efficiencies of up to 12.6% have already been demonstrated.²

Similar to $\text{Cu}(\text{In,Ga})\text{Se}_2$ solar cells, kesterite-based solar cells often feature non-stoichiometric absorber layers that are typically Cu-poor and Zn-rich.^{2,3} In the following, we will use the acronym CZTSe for any quaternary compound consisting of Cu, Zn, Sn, and Se, independent of its composition. In contrast to Cu-poor $\text{Cu}(\text{In,Ga})\text{Se}_2$,^{4,5} however, non-stoichiometric CZTSe is prone to the occurrence of a number of binary and ternary secondary phases such as ZnSe, SnSe/SnSe₂, CuSe/Cu₂Se, or Cu₂SnSe₃. These secondary phases, especially those with a bandgap energy smaller than that of CZTSe, have detrimental effects on the device performance and are discussed as one of the factors currently limiting the conversion efficiency of kesterite-based thin film solar cells.^{6,7} Furthermore, the presence of secondary phases leads to a discrepancy between the integral layer composition and the composition of the actual CZTSe. The latter, however, is crucial for the device performance since the type and concentration of point defects and defect clusters associated with a certain non-stoichiometry significantly affect the electrical properties of the CZTSe.^{8–10} Detailed information about the nature, quantity, and spatial distribution of secondary phases and a precise determination of the CZTSe stoichiometry are thus crucial in order to further improve the conversion efficiency of kesterite-based solar cells. In this

study, we applied high-resolution X-ray fluorescence (XRF) analysis using a synchrotron nanobeam to study the local composition of a highly non-stoichiometric Cu-Zn-Sn-Se layer chosen as an exemplary case. Apart from various secondary phases that all coexist within an area of only a few micrometers, we find that the local compositions of the actual CZTSe differ tremendously from the integral layer composition. An estimation of the defects present in the material based on the integral composition is thus thoroughly misleading in such a case. Consequently, the integral composition is not a reliable measure for characterizing the CZTSe in highly non-stoichiometric Cu-Zn-Sn-Se absorbers, and care has to be taken when relating it to other electrical or optical properties including the device performance.

The Cu-Zn-Sn-Se layer was grown by sequential selenization of a metallic precursor.¹¹ To that end, a Cu/Sn/Cu/Zn multilayer was deposited onto Mo-coated soda lime glass by magnetron sputtering. Subsequently, the metallic precursor was annealed in Se + Sn atmosphere, using a graphite box, in a two-stage process at 400 °C and 550 °C for 30 min and 15 min, respectively. The sample was then naturally cooled down from 550 °C to 300 °C keeping the lid of the furnace closed, which takes about one hour. Subsequently, the lid of the furnace was opened, and the sample was quenched to room temperature. The metallic layers of the initial glass/Mo/Cu/Sn/Cu/Zn stack show good uniformity; however, this type of precursor can induce the formation of non-uniform domains due to the segregation of bronze (Cu-Sn) and brass (Cu-Zn) alloys.¹² The integral layer composition was determined by standard XRF analysis and was found to be intentionally very Zn-rich and extremely Cu-poor with $\text{Zn}/\text{Sn} = 1.37$ and $\text{Cu}/(\text{Zn}+\text{Sn}) = 0.55$, in order to promote the formation of secondary phases. Grazing incidence X-ray

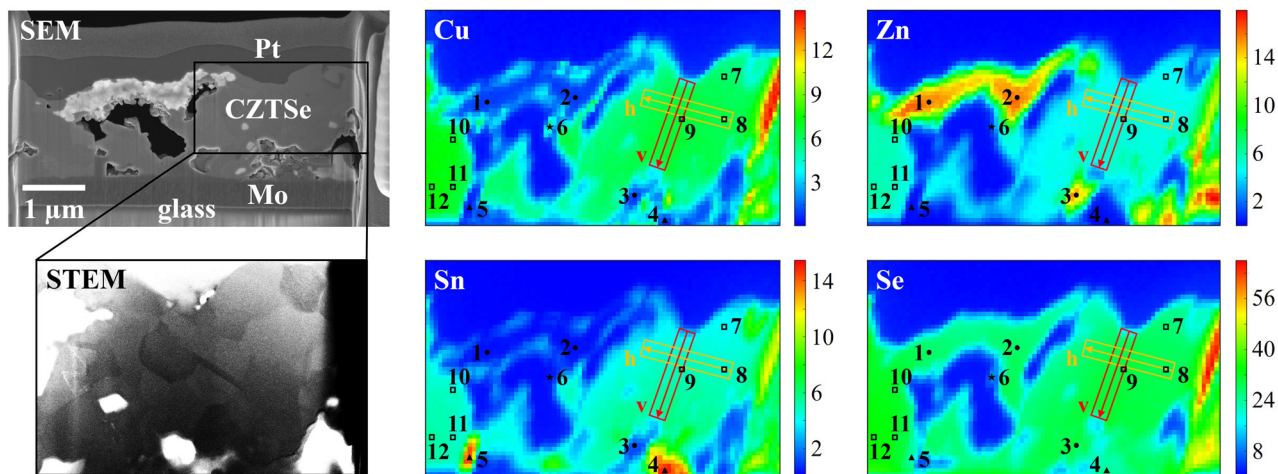


FIG. 1. Scanning electron micrograph of the cross section lamella (SEM, top left) together with the X-ray fluorescence maps of Cu, Zn, Sn, and Se. The color bars are labelled in 10^3 counts/s. The scanning transmission electron micrograph (STEM, bottom left) clearly reveals the CZTSe grain structure. Compositional line scans are shown in Figure 2, and the stoichiometry at the spots 1–12 is listed in Table I.

diffraction measurements (GIXRD) showed that the main structure of the layer is the kesterite type crystal structure. Additionally, a substantial fraction of SnSe is also present (see [supplementary material](#)). The detection of ZnSe by GIXRD is extremely difficult in this case and suffers from large uncertainties with regard to quantification. It can therefore be assumed that the Cu-Zn-Sn-Se layer consists of CZTSe regions (in the following called domains) that feature the kesterite type structure (CZTSe kesterite) and of SnSe/SnSe₂ and potentially ZnSe secondary phases. A thin cross section lamella of approximately 270 nm thickness was prepared using a focused ion beam system.¹³ Figure 1 presents a scanning electron micrograph of the lamella showing the glass substrate, the Mo layer, the Cu-Zn-Sn-Se layer, and a Pt protective layer deposited during the lamella preparation, while the scanning transmission electron micrograph (STEM) of the high-lighted CZTSe area reveals irregular grains of some hundred nanometers in size.

High-resolution XRF measurements were performed at the ID16B station of the European Synchrotron (ESRF) in Grenoble, France.¹⁴ The beam energy was set to 29.34 keV, while the beam spot size was 47×51 nm². The lamella was moved through the beam horizontally and vertically in 70 nm steps. At each spot, a full XRF spectrum was recorded using a single-element SII Nano Technology Vortex-90EX silicon drift detector. Plotting the number of counts associated with a certain fluorescence line as a function of the beam position yields a spatial intensity map of the corresponding element.¹³ Furthermore, fitting the individual XRF spectra using the software PyMca (Ref. 15) provides the elemental composition of the material at different spots of the lamella (see [supplementary material](#) for details). Given its thickness of approximately 270 nm, averaging over regions with different compositions or phases along the beam direction is strongly reduced compared to plan-view XRF analysis, thereby providing reliable information about the local chemistry at the submicrometer scale. In addition, the information depths of the Cu, Zn, Sn, and Se fluorescence photons are about tens of microns at 29.34 keV.¹⁶

Figure 1 presents the XRF intensity maps obtained for Cu, Zn, Sn, and Se. The morphology of the Cu-Zn-Sn-Se layer as seen in the scanning electron micrograph is readily apparent in the XRF maps despite a slight distortion due to a drift of the lamella during the measurement. The Se map further displays a homogeneous XRF intensity across the entire Cu-Zn-Sn-Se layer with only the holes and the edge of the lamella as exceptions. In contrast, the Cu, Zn, and Sn maps all exhibit pronounced intensity variations. Comparing the different maps, it becomes apparent that in some regions, an increased intensity for one of the cations corresponds to a nearly complete absence of the other two cations, clearly indicating the presence of binary secondary phases (spots 1–6 in Figure 1). Note that XRF provides information about the chemical composition of the material and thus about the co-localization of elements. It does not provide a structural analysis as obtained with X-ray diffraction or X-ray absorption spectroscopy nor a thermodynamical phase analysis. However, the formation of secondary binary phases in off-stoichiometric CZTSe was already demonstrated using these techniques. Therefore, we assume that Cu, Zn, or Sn atoms co-localized with Se form the corresponding binary compounds CuSe/Cu₂Se, ZnSe, or SnSe/SnSe₂. Fitting the corresponding XRF spectra provides the elemental compositions listed in Table I. Spots 1, 2, and 3 are located in ZnSe-like binary phases with small admixtures of Cu and Sn, while

TABLE I. Compositional analysis for different spots of the cross section lamella as indicated in Figure 1. The relative uncertainties of the atomic percentages are 1%–2%, while the absolute uncertainties of the Zn/Sn and Cu/(Zn+Sn) ratios are ± 0.05 and ± 0.02 , respectively.

Secondary phases		CZTSe		
Spot	Composition	Spot	Zn/Sn	Cu/(Zn+Sn)
1	Zn _{0.96} (Cu _{0.08} Sn _{0.01})Se	7	2.03	1.04
2	Zn _{0.99} (Cu _{0.07} Sn _{0.01})Se	8	1.81	1.00
3	Zn _{0.87} (Cu _{0.08} Sn _{0.05})Se	9	1.81	0.97
4	Sn _{0.63} (Cu _{0.08} Zn _{0.02})Se	10	2.17	1.00
5	Sn _{0.58} (Cu _{0.05} Zn _{0.02})Se	11	2.04	1.01
6	Cu _{1.48} (Zn _{0.17} Sn _{0.04})Se	12	1.99	1.00

spots 4 and 5 correspond to SnSe/SnSe₂-like binary phases with admixtures of Cu and Zn. Alternatively, the small amounts of the other two cations could originate from a small amount of kesterite behind or in front of the binary phase when viewed along the X-ray beam direction. Most surprisingly, though, spot 6 presents a small CuSe/Cu₂Se-like binary phase with admixtures of Zn and Sn in spite of the extremely low overall Cu content of Cu/(Zn+Sn) = 0.55. All three binary phases are thus present in the Cu-Zn-Sn-Se layer and coexist within an area that is only a few micrometers in size. Strong lateral compositional variations on the micrometer scale were also observed for this sample (see [Supplementary Material](#)) and other sequentially produced CZTSe thin films in plan-view geometry.¹⁷ However, our methodology allows the unambiguous identification of binary phases due to the small thickness of the cross section lamella. In the present case, the dimensions of these binary secondary phases range from about 100 nm up to 1 or 2 μm. The ZnSe-like phases are located mostly at the top of the layer, whereas the SnSe/SnSe₂-like phases are found at the CZTSe/Mo interface. This is most likely due to the initial glass/Mo/Cu/Sn/Cu/Zn precursor configuration and reflects the reaction kinetics during the selenization.

Some regions of the XRF maps, particularly at the very left and in the middle right, show roughly homogeneous intensities of all four elements and thus represent the actual CZTSe kesterite observed with X-ray diffraction. The local composition was determined for different spots within these regions, and the corresponding cation ratios are listed in Table I (spots 7–12 in Figure 1). Most remarkably, the Cu/(Zn+Sn) ratio varies between 0.97 and 1.04, whereas the Zn/Sn ratio ranges from 1.8 to 2.2. The compositions of these kesterite domains in this part of the sample from which the lamella was prepared are thus extremely Zn-rich and Sn-poor but not Cu-poor in striking contrast to the integral layer composition of Zn/Sn = 1.37 and Cu/(Zn+Sn) = 0.55. Note that here we define the term “Cu-poor” as Cu/(Zn+Sn) < 1, similar to the case of Cu(In,Ga)Se₂ where “Cu-poor” is defined as Cu/(In+Ga) < 1. For the latter, being Cu-poor is directly related to the presence of Cu vacancies. In contrast, for quaternary CZTSe kesterite, the presence of Cu vacancies depends on both the Cu/(Zn+Sn) and the Zn/Sn ratio and can be deduced from the different defect types in the Cu-poor/Zn-rich and Cu-poor/Zn-poor quadrants of the cation ratio plot as discussed below.^{18–20} Therefore, Cu-poor CZTSe kesterite does not automatically feature Cu vacancies. The surprisingly low Sn content most likely corresponds to the formation of Sn secondary phases (SnSe and SnSe₂) due to the imposed very Cu-poor and Zn-rich starting conditions. This is also supported by the GIXRD measurement, which detected a substantial fraction of SnSe. As mentioned above, non-uniformities and secondary phases are to be expected for this type of non-equilibrium process and metallic precursor composition. Therefore, a discrepancy between the integral layer composition and the local CZTSe compositions is not surprising. The extent of this discrepancy is, however, striking and demonstrates just how much local and integral compositions may differ. We note that these results strongly depend on the details of the synthesis and that different growth processes are likely to yield different

compositional properties of the final thin films. Nevertheless, compositional variations and secondary phase segregation on a nanometer scale were also observed for co-evaporated CZTSe thin films using atom probe tomography and similarly resulted in a remarkable discrepancy between the local CZTSe composition and the integral layer composition.²¹

To study the spatial compositional variations of the CZTSe domains in more detail, two line scans were extracted, one horizontally and one vertically, as shown in Figure 1. The resulting Zn/Sn and Cu/(Zn+Sn) ratios are plotted in Figure 2. The Cu content of the CZTSe decreases with increasing depth from Cu/(Zn+Sn) = 1.06 near the surface to 0.90 closer to the CZTSe/Mo interface, as shown in the vertical scan. The layer thus features both Cu-rich and Cu-poor CZTSe regions. The Zn content also decreases with increasing depth, but the change is much more pronounced than for Cu. The Zn/Sn ratio falls from 2.06 near the surface to 1.54 closer to the CZTSe/Mo interface, which is again related to the sequence of metal layers in the initial precursor featuring Zn at the top and Sn closer to the Mo interface. Laterally, the Cu content is nearly constant across the area investigated and exhibits only slight variations that fall within the experimental uncertainty. In contrast, the Zn/Sn ratio rises from 1.8 to 2.0 along the horizontal scan. The CZTSe kesterite of this part of the sample thus accommodates significant compositional variations on a nanometer scale. Carefully designed and optimized compositional gradients may strongly enhance the solar cell performance as demonstrated extensively for Cu(In,Ga)(Se,S)₂ devices.²² Unwanted and unfavorable heterogeneity, however, may severely limit the conversion efficiency and needs to be avoided.

When studying CZTSe thin films and solar cells based thereon, it is a common practice to correlate the electrical or optical properties investigated, including the device performance, with the integral composition of the Cu-Zn-Sn-Se layer. Cu-poor, Zn-rich compositions with $0.7 \leq \text{Cu}/(\text{Zn}+\text{Sn}) \leq 0.9$ and $1.1 \leq \text{Zn}/\text{Sn} \leq 1.4$ are usually considered optimal since the resulting Cu vacancies (V_{Cu}) provide beneficial p-type doping, while a Zn/Sn ratio larger than one

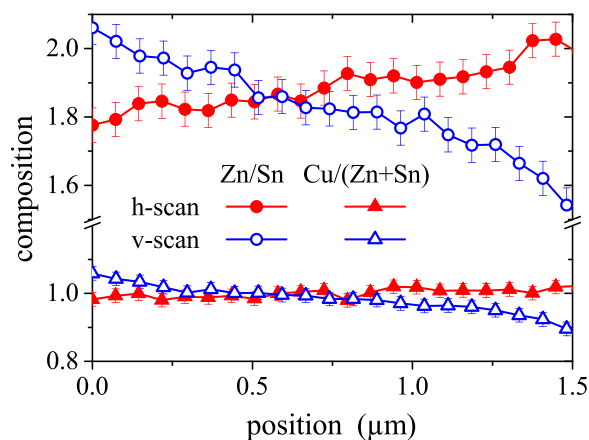


FIG. 2. Local CZTSe composition given by the Zn/Sn and Cu/(Zn+Sn) ratios as a function of the beam position along the horizontal (h) and vertical (v) line scans indicated in Figure 1. Each data point represents the average over four pixels corresponding to 280 nm. Note the break in scale for the composition.

suppresses the formation of harmful Sn_{Zn} antisite defects.^{3,8} To anticipate the type of point defects and defect clusters associated with a certain composition, different types of non-stoichiometry (A-F) have been proposed based on different cation substitution reactions, assuming charge balance and unchanging valence states.^{18–20} Figure 3 plots Zn/Sn versus $\text{Cu}/(\text{Zn}+\text{Sn})$ for these types of non-stoichiometry together with the integral layer and local CZTSe compositions determined in this work. Based on the integral composition of the entire layer, the kesterite would clearly be assigned A-type featuring V_{Cu} and Zn_{Cu} antisites. In contrast, the actual local CZTSe domains observed in the lamella can be expressed as a mixture of B- and F-type. The former is characterized by Zn_{Cu} and Zn_{Sn} antisites, while the latter features Zn_{Sn} and Cu_{Sn} antisites plus Cu and Zn interstitials (Cu_i and Zn_i , respectively).

Given the almost ideal $\text{Cu}/(\text{Zn}+\text{Sn})$ ratio for the local composition, it could also be conceived that in this case, the main cation substitution reaction occurs between Zn and Sn only. We therefore propose the substitution $\text{Sn}^{4+} \rightarrow \text{Zn}_{\text{Sn}}^{2+} + \text{Zn}_i^{2+}$ with the corresponding formula $\text{Cu}_2\text{Zn}_{1+2x}\text{Sn}_{1-x}\text{Se}_4$ for Zn-rich conditions (called G-type) and the substitution $2\text{Zn}^{2+} \rightarrow \text{Sn}_{\text{Zn}}^{4+} + \text{V}_{\text{Zn}}$ with the corresponding formula $\text{Cu}_2\text{Zn}_{1-2x}\text{Sn}_{1+x}\text{Se}_4$ for Sn-rich conditions (called H-type) as shown in Figure 3. The formation energy of the resulting defect pair in H-type non-stoichiometry is similar to those of other non-stoichiometry types previously reported, while no value is given for the G-type defect pair.²³ As seen in Figure 3, the local CZTSe compositions of the lamella correspond to a mixture of G- and F-types involving the acceptor levels of Zn_{Sn} , the deep acceptor levels of Cu_{Sn} ranging up to more than 400 meV above the valence band maximum, the shallow donor level of Cu_i , and two deep Zn_i donor levels located approximately 300 meV below the conduction band minimum.²³ In contrast, V_{Cu} and Zn_{Cu} associated with A-type non-stoichiometry lead to shallow acceptor and donor levels, respectively.²³ As a consequence, very different types of defects and very different defect levels are anticipated, depending on whether the integral or the local composition is considered. Correlating electronic or optical properties

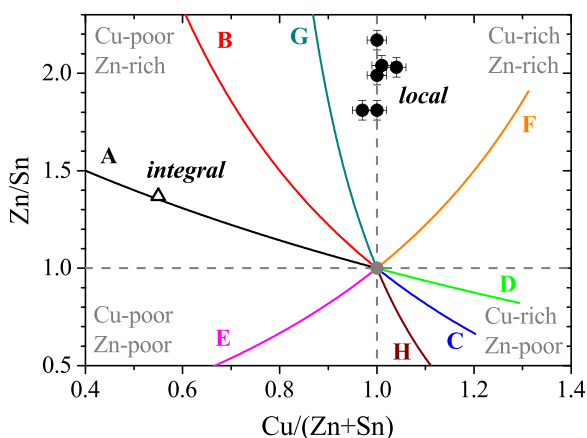


FIG. 3. Cation ratio plot for CZTSe including different types of non-stoichiometry previously reported (A–F) and introduced here (G, H). The local CZTSe compositions determined for the different spots indicated in Figure 1 and listed in Table I are given together with the integral composition of the entire Cu-Zn-Sn-Se layer.

with the integral layer composition of highly non-stoichiometric CZTSe can thus easily lead to misinterpretations and unsound conclusions. Even if the nature and amount of secondary phases are properly determined and accounted for as done, for example, by X-ray absorption spectroscopy,²⁴ there may remain considerable uncertainty about the exact composition of the CZTSe domains due to possible spatial fluctuations as shown in Figure 2. Interestingly, Just *et al.* report that the Zn/Sn ratio of the actual CZTSe kesterite in their co-evaporated samples never exceeds one in strong contrast to the ratios listed in Table I.²⁴ This could indicate that, depending on the synthesis route, the preparation conditions, and the initial elemental concentrations, the kesterite type crystal structure can accommodate a variety of CZTSe compositions different from the stoichiometric one. The large existence range of the kesterite structure for CZTSe, concurrent with binary secondary phases or not, was also clearly demonstrated by X-ray diffraction analysis of CZTSe powder samples covering a wide compositional range.²⁰ Note, however, that compositional and structural methods of analysis such as X-ray fluorescence spectroscopy, X-ray diffraction, or X-ray absorption spectroscopy do not provide information about the thermodynamical properties and thus cannot elucidate the phase structure of this existence region of CZTSe kesterite.

In conclusion, we applied high-resolution XRF analysis using a synchrotron nanobeam to study the spatially resolved elemental composition of a CZTSe cross section lamella cut from a layer with an integral composition that is very Cu-poor and Zn-rich. We find ZnSe -, $\text{SnSe}/\text{SnSe}_2$ -, and $\text{CuSe}/\text{Cu}_2\text{Se}$ -like binary secondary phases all coexisting within an area of only a few micrometers in size. The actual CZTSe domains observed in the lamella exhibit local compositions that are strikingly different from the overall layer composition being extremely Zn-rich and Sn-poor yet only slightly or not at all Cu-poor. Anticipating the kinds of defects present in these CZTSe kesterite domains based on the integral layer composition will thus lead to wrong assumptions about the material properties. Consequently, the integral layer composition is not a reliable measure for the characterization of highly non-stoichiometric CZTSe, and care has to be taken when relating it to other material properties, including the device performance.

See [supplementary material](#) for additional information on the GIXRD measurement and the XRF study including plan-view XRF maps and full XRF spectra.

We acknowledge the ESRF for provision of synchrotron radiation facilities and thank D. Solomon, A. Johannes, and S. Schönherr for support during the XRF measurements. This work was funded by ESRF, DFG (Deutsche Forschungsgemeinschaft) under Grant No. SCHN 1283/2-1, BMBF (Bundesministerium für Bildung und Forschung) under the “nano@work” project (Grant No. 05 K16SJ1), KESTCELLS 316488, FP7-PEOPLE-2012 ITN, Multi-ITN project, and MINECO (Ministerio de Economía y Competitividad de España) under the NASCENT Project (ENE2014-56237-C4-1-R). The authors from IREC belong

to the M-2E (Electronic Materials for Energy) Consolidated Research Group and the XaRMAE Network of Excellence on Materials for Energy of the “Generalitat de Catalunya”. S.G. thanks the Government of Spain for the FPI fellowship (BES-2014-068533) and E.S. for the “Ramón y Cajal” fellowship (RYC-2011-09212).

- ¹P. Jackson, R. Wuerz, D. Hariskos, E. Lotter, W. Witte, and M. Powalla, *Phys. Stat. Sol. RRL* **10**, 583 (2016).
- ²W. Wang, M. T. Winkler, O. Gunawan, T. Gokmen, T. K. Todorov, Y. Zhu, and D. B. Mitzi, *Adv. Energy Mater.* **4**, 1301465 (2014).
- ³A. Fairbrother, M. Dimitrievska, Y. Sánchez, V. Izquierdo-Roca, A. Pérez-Rodríguez, and E. Saucedo, *J. Mater. Chem. A* **3**, 9451 (2015).
- ⁴C. Stephan, S. Schorr, M. Tovar, and H.-W. Schock, *Appl. Phys. Lett.* **98**, 091906 (2011).
- ⁵C. Stephan, T. Scherb, C. A. Kaufmann, S. Schorr, and H.-W. Schock, *Appl. Phys. Lett.* **101**, 101907 (2012).
- ⁶S. Siebentritt and S. Schorr, *Prog. Photovoltaics: Res. Appl.* **20**, 512 (2012).
- ⁷A. Kanevce, I. Repins, and S.-H. Wei, *Sol. Energy Mater. Sol. Cells* **133**, 119 (2015).
- ⁸X. Liu, Y. Feng, H. Cui, F. Liu, X. Hao, G. Conibeer, D. B. Mitzi, and M. Green, *Prog. Photovoltaics: Res. Appl.* **24**, 879 (2016).
- ⁹S. Bourdais, C. Choné, B. Delatouche, A. Jacob, G. Larramona, C. Moisan, A. Lafond, F. Donatini, G. Rey, S. Siebentritt, A. Walsh, and G. Dennler, *Adv. Energy Mater.* **6**, 1502276 (2016).
- ¹⁰J. Márquez, M. Neuschitzer, M. Dimitrievska, R. Gunder, S. Haass, M. Werner, Y. E. Romanyuk, S. Schorr, N. M. Pearsall, and I. Forbes, *Sol. Energy Mater. Sol. Cells* **144**, 579 (2016).
- ¹¹S. Giraldo, M. Neuschitzer, T. Thersleff, S. López-Marino, Y. Sánchez, H. Xie, M. Colina, M. Placidi, P. Pistor, V. Izquierdo-Roca, K. Leifer, A. Pérez-Rodríguez, and E. Saucedo, *Adv. Energy Mater.* **5**, 1501070 (2015).
- ¹²D. M. Berg, A. Crossay, J. Guillot, V. Izquierdo-Roca, A. Pérez-Rodríguez, S. Ahmed, H. Deligianni, S. Siebentritt, and P. J. Dale, *Thin Solid Films* **573**, 148 (2014).
- ¹³Ph. Schöppe, C. S. Schnohr, M. Oertel, A. Kusch, A. Johannes, S. Eckner, M. Burghammer, G. Martínez-Criado, U. Reislöhner, and C. Ronning, *Appl. Phys. Lett.* **106**, 013909 (2015).
- ¹⁴G. Martínez-Criado, J. Villanova, R. Tucoulou, D. Salomon, J.-P. Suuronen, S. Labouré, C. Guilloud, V. Valls, R. Barrett, E. Gagliardini, Y. Dabin, R. Baker, S. Bohic, C. Cohen, and J. Morse, *J. Synchrotron Radiat.* **23**, 344 (2016).
- ¹⁵V. A. Solé, E. Papillon, M. Cotte, Ph. Walter, and J. Susini, *Spectrochim. Acta, Part B* **62**, 63 (2007).
- ¹⁶L. Tröger, D. Arvanitis, K. Baberschke, H. Michaelis, U. Grimm, and E. Zschech, *Phys. Rev. B* **46**, 3283 (1992).
- ¹⁷A. Crossay, D. Colombara, M. Melchiorre, M. Guennou, B. G. Mendis, and P. J. Dale, *J. Mater. Chem. C* **4**, 4626 (2016).
- ¹⁸A. Lafond, L. Choubrac, C. Guillot-Deudon, P. Deniard, and S. Jobic, *Z. Anorg. Allg. Chem.* **638**, 2571 (2012).
- ¹⁹G. Gurieva, M. Dimitrievska, S. Zander, A. Pérez-Rodríguez, V. Izquierdo-Roca, and S. Schorr, *Phys. Status Solidi C* **12**, 588 (2015).
- ²⁰L. E. Valle Rios, K. Neldner, G. Gurieva, and S. Schorr, *J. Alloys Compd.* **657**, 408 (2016).
- ²¹T. Schwarz, O. Cojocar-Mirédin, P. Choi, M. Mousel, A. Redinger, S. Siebentritt, and D. Raabe, *Appl. Phys. Lett.* **102**, 042101 (2013).
- ²²A. Chirilă, S. Buecheler, F. Pianezzi, P. Bloesch, C. Gretener, A. R. Uhl, C. Fella, L. Kranz, J. Perrenoud, S. Seyrling, R. Verma, S. Nishiwaki, Y. E. Romanyuk, G. Bilger, and A. N. Tiwari, *Nat. Mater.* **10**, 857 (2011).
- ²³S. Chen, A. Walsh, X.-G. Gong, and S.-H. Wei, *Adv. Mater.* **25**, 1522 (2013).
- ²⁴J. Just, C. M. Sutter-Fella, D. Lützenkirchen-Hecht, R. Frahm, S. Schorr, and T. Unold, *Phys. Chem. Chem. Phys.* **18**, 15988 (2016).